
Cryogenic Target Performance and Implosion Physics Studies on OMEGA

Introduction

The goal of inertial confinement fusion (ICF)^{1,2} is to implode a spherical target to achieve high compression of the fuel and high temperature of the hot spot to trigger ignition and maximize the thermonuclear energy gain. Both direct- and indirect-drive concepts of ICF rely on targets with thick, cryogenic deuterium–tritium (DT) shells for ignition.^{1–3} While target designs vary in their details, these concepts have common basic physics such as ablator and fuel compressibility, energy coupling and transport, hydrodynamic instabilities, shock tuning, and preheating. Recent OMEGA cryogenic D₂ experiments demonstrated ignition-relevant fuel compression with a neutron-averaged areal density of ~ 200 mg/cm² (Refs. 4 and 5). This corresponds to an estimated peak fuel density of ~ 100 g/cm³, $\sim 500\times$ higher than initial cryogenic ice density. These experiments were conducted at peak drive intensities of $\sim 5 \times 10^{14}$ W/cm² using 10- μ m-thick plastic ablators with an implosion velocity of $\sim 2.4 \times 10^7$ cm/s (Refs. 4 and 5). To achieve an ignition-relevant implosion velocity of $\sim 4 \times 10^7$ cm/s, the peak drive intensity must be increased to $\sim 10^{15}$ W/cm² (Refs. 3 and 4). Recent direct-drive ICF research on OMEGA focused on understanding the physics of this high-intensity regime. Understanding the dynamics of target implosion is essential to all ignition target designs, whether directly or indirectly driven. This article reviews the results obtained over this past year in the physics of cryogenic target implosions, including energy coupling and transport, hydrodynamic instabilities, compressibility, shock timing, and preheating.

The following sections (1) show the importance of non-local electrons in modeling laser coupling and energy transport; (2) present recent results from experiments that show stabilization of hydrodynamic instabilities at peak intensities of $\sim 10^{15}$ W/cm²; and (3) describe compressibility experiments performed in plastic ablators, shock-timing experiments, compression results from cryogenic D₂ spherical implosions, and spherical experiments in Si-doped plastic ablators. The final section summarizes these results.

Energy Coupling and Transport

Acceleration experiments with planar plastic foils were conducted to study energy coupling and transport in plastic ablators.⁶ In these experiments, 2.5-mm-diam, 20- μ m-thick CH targets were driven with a 1-ns square pulse shape at a peak laser intensity of $\sim 10^{15}$ W/cm². The targets were driven with 12 overlapped beams using all standard OMEGA beam-smoothing techniques, including distributed phase plates (DPP's),⁷ polarization smoothing (PS),⁸ and smoothing by spectral dispersion (SSD).⁹ The target acceleration was measured using side-on radiography with a streak camera using ~ 2 -keV x rays from a dysprosium sidelighter and compared with two-dimensional (2-D) *DRACO* simulations.⁶ The simulations used a local model for electron transport¹⁰ with a time-dependent flux limiter derived from a one-dimensional (1-D) nonlocal thermal-electron-transport model.¹¹ The nonlocal model solves the Boltzman equation with the Krook's collision operator and an appropriate electron-deposition length. It gives an effective time-dependent flux limiter, defined as the ratio of nonlocal heat flux to the free-stream heat flux.¹¹

The measured target trajectory [Fig. 117.9(a)] is in good agreement with the simulated trajectory using the effective time-dependent flux limiter shown in Fig. 117.9(b). Reference 6 shows that the measured target trajectories are in good agreement with nonlocal model predictions over the broad range of intensities from $\sim 2 \times 10^{14}$ to 1×10^{15} W/cm². Predictions using a local model of thermal transport with a constant flux limiter of $f = 0.06$ (Ref. 10) (previous standard model for OMEGA experiments) are in good agreement with experiments at intensities below $\sim 5 \times 10^{14}$ W/cm², but break down at peak intensities $\sim 10^{15}$ W/cm², as shown in Fig. 117.9(a). These results indicate that nonlocal effects are critical for modeling energy coupling and transport in direct-drive-ignition designs using high-intensity UV lasers. Experiments using green and IR lasers have shown that nonlocal effects were important even at much lower intensities of $\sim 1 \times 10^{14}$ W/cm² (Refs. 12 and 13).

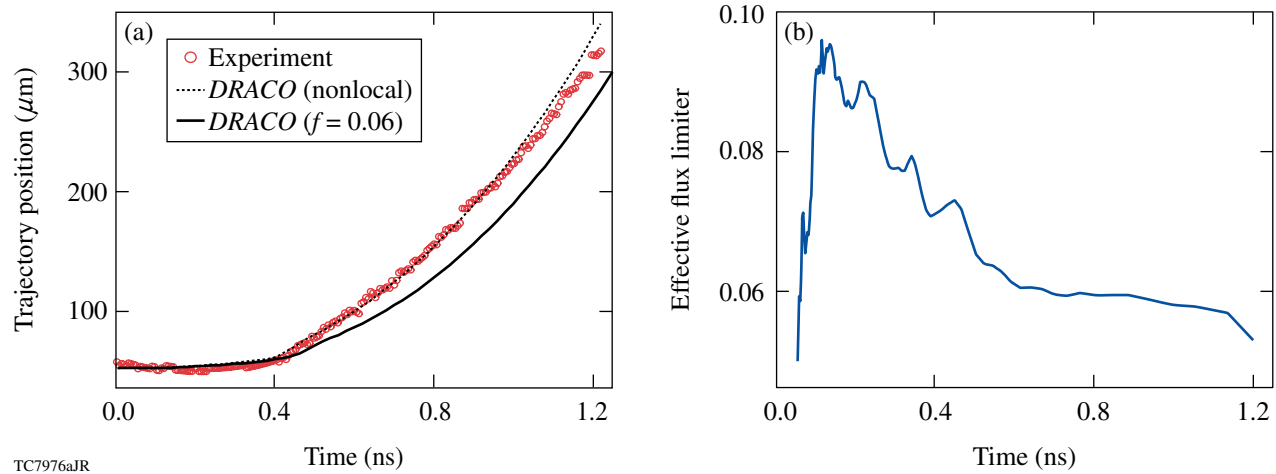


Figure 117.9

(a) Measured (circles) and simulated target trajectories using a flux limiter of $f = 0.06$ (solid line) and an effective flux limiter derived from the nonlocal model (dotted line), shown in (b).

Hydrodynamic Instability Experiments

The nonlocal model for electron thermal transport predicts target decompression at the ablation front¹¹ relative to prediction of the local model.¹⁰ The decompression at the ablation front is caused by heating from the high-energy tail of the electron distribution. The decompression at the ablation surface reduces the growth rate of Rayleigh–Taylor (RT) instability.^{12–15} In the linear stage of RT instability, the growth rate as a function of modulation wave number k in plastic targets is given by the dispersion relation¹⁶

$$\gamma(k) = 0.94 \left[kg / (1 + kL_n) \right]^{0.5} - 1.5 kV_a, \quad (1)$$

where g is the target acceleration, V_a is the ablation velocity, and L_n is the density scale length. The growth rate is proportional to the first acceleration term and is reduced by the second stabilizing term $-1.5 kV_a$, caused by material ablation. When the target is decompressed, the ablation velocity increases, resulting in a reduced RT growth rate. This reduction is stronger for modulations with high wave numbers (shorter wavelengths). This was experimentally observed in 20- μm -thick, planar CH targets driven with various square drive pulses.^{14,15}

In this work, 20- μm -thick CH targets were driven with 12 overlapped beams with full beam smoothing including DPP's,⁷ PS,⁸ and SSD.⁹ The RT growth of preimposed 2-D modulations was measured with through-foil, x-ray radiography^{14,15} using ~ 1.3 -keV x rays from a uranium backlighter.

In the RT experiments, the 2-D preimposed modulations had wavelengths of 20, 30, and 60 μm , with initial amplitudes of 0.05, 0.05, and 0.125 μm , respectively. Results of RT growth experiments are shown in Fig. 117.10 for a 1-ns drive at an intensity of $\sim 1 \times 10^{15}$ W/cm² [Figs. 117.10(a)–117.10(c)] and a 1.6-ns drive at an intensity of $\sim 5 \times 10^{14}$ W/cm² [Figs. 117.10(d)–117.10(f)]. The experimental data at a 60- μm wavelength are weakly affected by the stabilizing term $-1.5 kV_a$ [Figs. 117.10(a) and 117.10(d)]. This modulation grows more rapidly at a drive intensity of $\sim 10^{15}$ W/cm² than at $\sim 5 \times 10^{14}$ W/cm². This indicates that the acceleration is higher at high intensity, as expected. At an intensity of $\sim 5 \times 10^{14}$ W/cm² the short-wavelength modulations (at wavelengths of 20 μm and 30 μm) grow faster than the long, 60- μm -wavelength modulation. At a high intensity of 1×10^{15} W/cm², this trend is reversed: the 60- μm -wavelength modulation grows faster than the 30- μm perturbation, with the 20- μm -wavelength perturbation completely stabilized.

This stabilization is consistent with the increased ablation velocity and density scale length at high intensity predicted by the nonlocal electron transport model.^{11,14} The stabilization is also correlated with the hot-electron signal from two-plasmon-decay (TPD) instability.^{14,17,18} This signal becomes detectable at intensities above $\sim 5 \times 10^{14}$ W/cm², similar to previous experiments.^{4,19} The relationship between the x-ray emission and the target preheat is still under investigation. The strong measured RT growth stabilization reduces the requirements for mitigation of the hydro-instability growth in direct-drive-ignition capsules

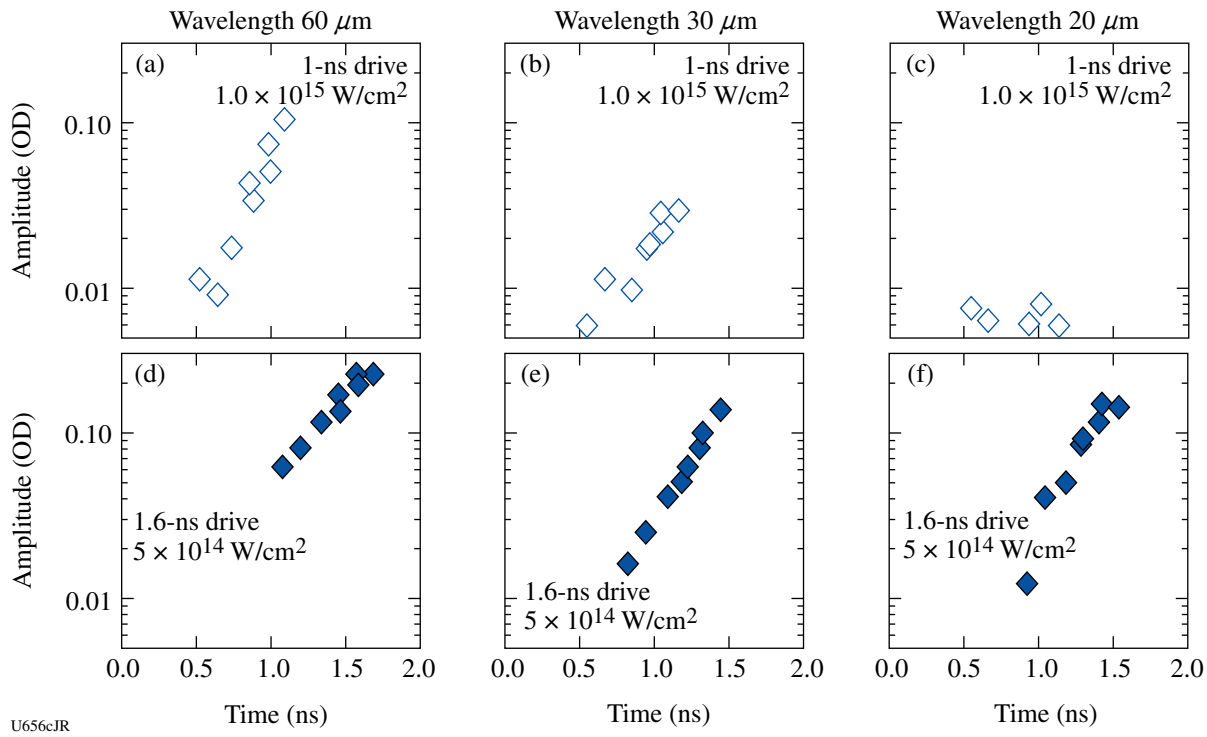


Figure 117.10

Optical-depth modulations versus time for a 1-ns square laser drive at an intensity of $\sim 1 \times 10^{15} \text{ W/cm}^2$ [(a), (b), and (c)], and with a 1.6-ns square laser drive at an intensity of $\sim 5 \times 10^{14} \text{ W/cm}^2$ [(d), (e), and (f)] with wavelengths of $60 \mu\text{m}$, $30 \mu\text{m}$, and $20 \mu\text{m}$, respectively.

at the National Ignition Facility (NIF).¹⁴ Future experiments will distinguish between nonlocal and hot-electron contributions to the ablation-surface preheating.

Plastic-Ablator Compressibility

Figure 117.11 shows a schematic of the plastic-ablator compressibility experiments²⁰ performed with $\sim 125\text{-}\mu\text{m}$ -thick, $\sim 280\text{-}\mu\text{m}$ -wide plastic planar targets driven with a high-compression, 3-ns-long shaped pulse at a peak drive intensity of $\sim 1 \times 10^{15} \text{ W/cm}^2$, as shown in Fig. 117.12(a). The targets were driven with 14 overlapped beams with full beam smoothing, including DPP's,⁷ PS,⁸ and SSD.⁹ The target compression was measured with x-ray, side-on radiography using an $\sim 6.4\text{-keV}$ iron sidelight. The 2-ns-long foot of the pulse sends a shock wave that compresses the ablator by $\sim 3\times$. The compression increases up to $\sim 9\times$ when the main shaped pulse sends a compression wave through the target. Figures 117.12(b) and 117.12(c) compare the measured and simulated optical-depth compression of the target. The shock and compression waves travel from right to left in these data. The predictions for (b) 2.3 ns and (c) 2.9 ns show good agreement with the experiment, confirming the compression of the plastic ablator by a shaped laser drive. These measurements validated

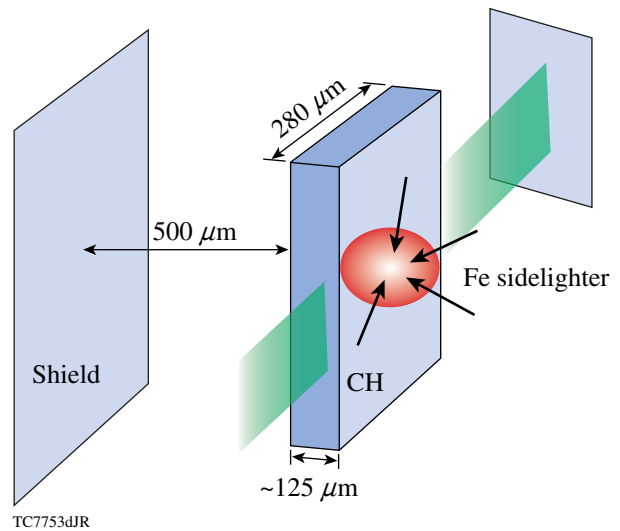


Figure 117.11

Experimental setup for plastic-ablator compressibility experiments performed with $\sim 125\text{-}\mu\text{m}$ -thick, $\sim 280\text{-}\mu\text{m}$ -wide plastic planar targets driven with 14 overlapped beams. The target compression was measured with x-ray, side-on radiography using an $\sim 6.4\text{-keV}$ iron sidelight.

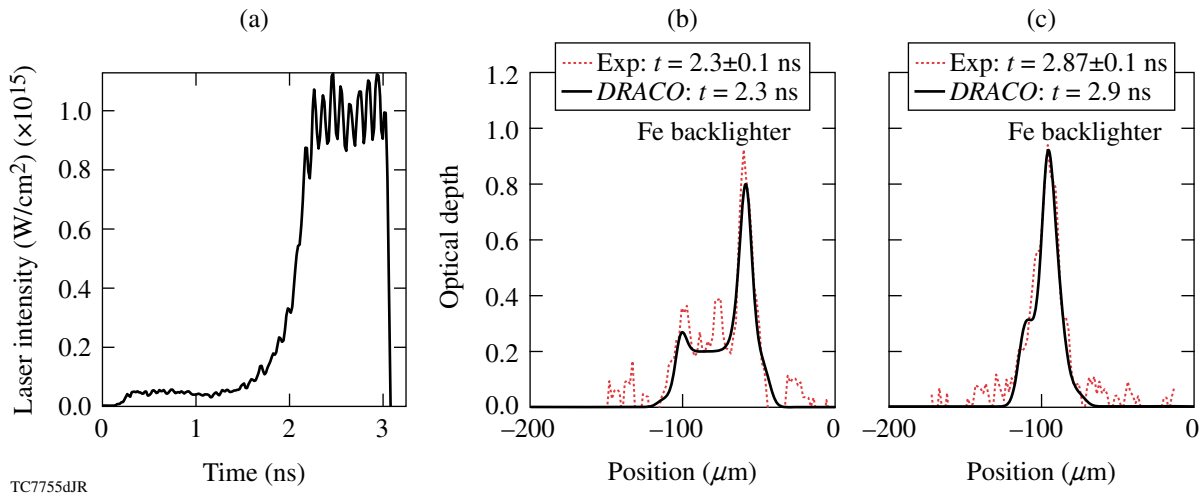


Figure 117.12

(a) High-compression, 3-ns-long laser pulse shape. The measured (dotted line) and simulated (solid line) optical-depth target compression at (b) 2.3 ns and (c) 2.9 ns. The shock and compression waves travel from right to left. The predictions show good agreement with measurements.

the hydrodynamics and equation of state (*SESAME*) of the shock and compression waves predicted by the 2-D hydrocode *DRACO*,²⁰ used to simulate the experiments. Similar experiments conducted at lower intensities of $\sim 5 \times 10^{14}$ W/cm^2 also showed agreement with hydro simulations, while experiments at an intensity of $\sim 1.5 \times 10^{15}$ W/cm^2 (higher than required for ignition on the NIF) showed target decompression that was correlated with the presence of hot electrons generated by TPD instability.²⁰

Shock Timing

Figure 117.13 shows a schematic of the shock-timing experiments performed with spherical 10- μm -thick CD shells filled with cryogenic D_2 liquid.²¹ The target cone makes it possible for the active shock breakout (ASBO)²² system to probe the shock waves in liquid deuterium. The experiments were performed with 36 overlapped OMEGA beams using all standard OMEGA beam-smoothing techniques, including DPP's,⁷ PS,⁸ and SSD.⁹ The diagnostics probed the central region of the target, which had the same illumination conditions as cryogenic spherical implosions. Figure 117.14(a) shows the pulse shape used during one of the experiments. The measured shock velocity as a function of time (solid curve) is shown in Fig. 117.14(b). The data are compared with the 1-D predictions, shown by the dotted curve. In the 1-D prediction, the picket pulse launches the first shock, which decays as it travels through the target. This is shown by the decreasing shock velocity as a function of time. As a compression wave is launched by the shaped laser pulse starting at ~ 1.2 ns, the shock velocity gradually decreases in the simulation. The measurements indicate that the

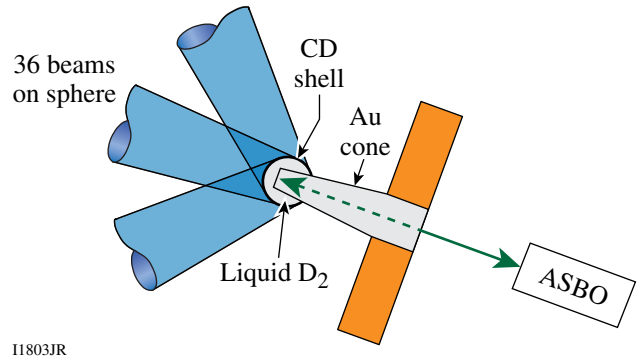


Figure 117.13

Schematic of shock-timing experiments consisting of spherical 10- μm -thick CD shells filled with liquid deuterium driven with 36 overlapped OMEGA beams. The targets have openings for active shock breakout (ASBO) diagnostics to probe shocks in liquid deuterium.

compression wave turns into a shock wave inside the target. The measured shock velocity from the first shock is smaller than predicted. This measurement suggests that energy coupling from the picket and low-intensity part of the pulse is reduced, compared to the simulation. The adiabat (the ratio of the plasma pressure to the Fermi pressure of a fully degenerate electron gas) of the CD shell and D_2 fuel is likely higher than simulated, leading to compression degradation in spherical implosions.

Since 1-D simulations incorrectly predict the shock timing, experimental measurements can be used to tune multiple hydrodynamic waves. Experimentally, it is easier to tune shock waves than compression waves because the multiple shock

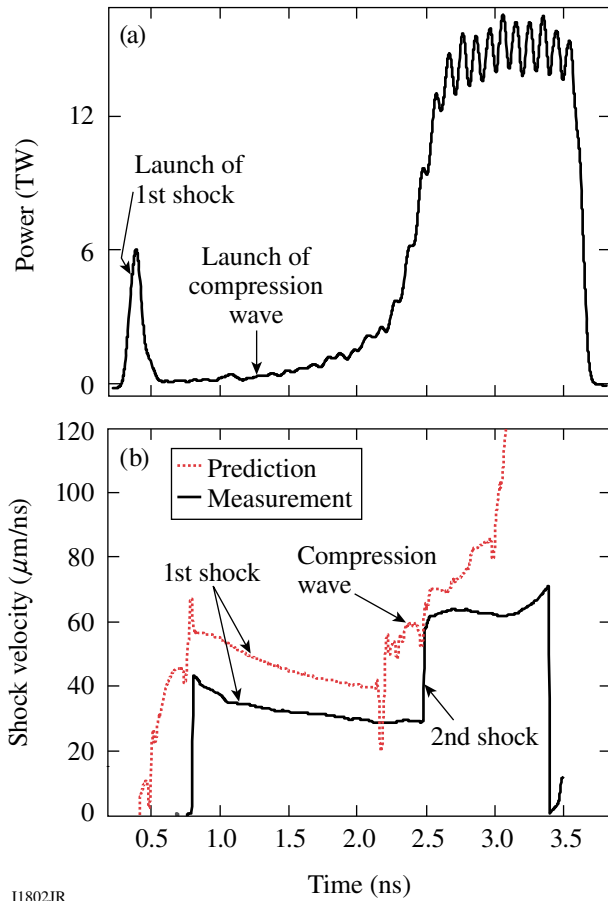


Figure 117.14

(a) The laser pulse shape for the continuous laser-pulse experiments. (b) The measured (solid line) and simulated (dotted line) shock velocities as a function of time.

waves are much easier to create and interpret. Figure 117.15(a) shows the double-picket pulse shape used for one such experiment and the measured shock velocity as a function of time [solid curve in Fig. 117.15(b)]. The data are compared with the 1-D prediction shown by the dotted curve. In the 1-D prediction, the first picket sends the first shock wave that decays as it travels through the target. The second picket sends a stronger second shock that travels faster and overtakes the first shock wave at ~ 2 ns. The main part of the pulse sends a third shock wave, which coalesces with the two earlier shocks at ~ 4 ns. The experiment shows that the shocks coalesce. The shock velocities are smaller, however, in the experiment, indicating that the shock coalescence events occur at different spatial locations than predicted. Future experiments will tune shock waves using triple-picket pulses with the square main pulse. This technique is similar to that used for shock tuning in indirect-drive-ignition designs.^{1,2,21}

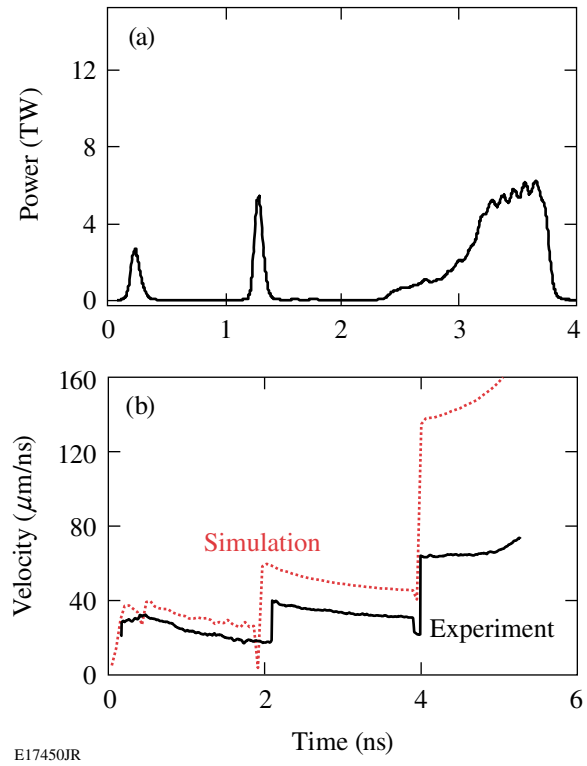


Figure 117.15

(a) The pulse shape for the double-picket, laser-pulse experiments. (b) The measured (solid line) and simulated (dotted line) shock velocities as a function of time.

Cryogenic-Target Compression

Figure 117.16 shows compression results obtained in spherical implosions with outer $10\text{-}\mu\text{m}$ -thick CD ablaters and inner $95\text{-}\mu\text{m}$ -thick cryogenic- D_2 -ice fuel shells. Figure 117.16(a) shows three examples of continuous laser pulses at a peak intensity range from $\sim 5 \times 10^{14}$ W/cm² to $\sim 8 \times 10^{14}$ W/cm². Figure 117.16(b) shows an example of a double-picket pulse at a peak intensity range of $\sim 9 \times 10^{14}$ W/cm². Figure 117.16(c) shows a comparison of the compression results obtained with these two types of laser pulses in which the neutron-averaged areal density was predicted to be ~ 250 mg/cm² if the shock pulses were properly timed. The highest compression with measured areal density in the range of 180 to 200 mg/cm² was obtained at the peak intensity of $\sim 5 \times 10^{14}$ W/cm². Two of the four data points at this intensity were presented in Ref. 5, while the other two were obtained recently, showing a good repeatability of these results. The neutron yield varied by a factor of ~ 5 because of variations of the inner ice roughness in these implosions. While the yield varied, the areal density did not, showing that the areal density is a robust measure of target compression, as previously shown in plastic implosions.²³

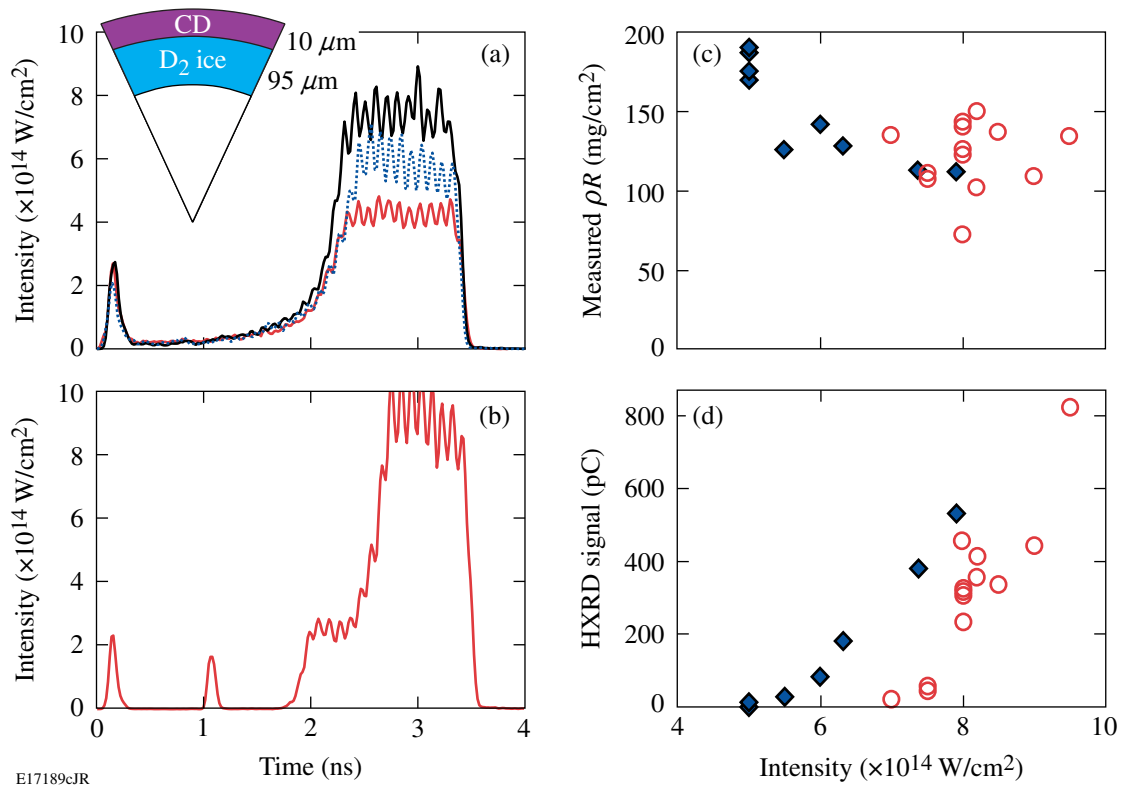


Figure 117.16

(a) Schematic of spherical targets used in implosions consisting of outer 10- μm -thick CD ablaters and 95- μm -thick inner cryogenic-D₂-ice shells driven with continuous laser pulses at peak intensities ranging from $\sim 5 \times 10^{14} \text{ W/cm}^2$ to $\sim 8 \times 10^{14} \text{ W/cm}^2$. (b) An example of a double-picket laser pulse with a peak intensity of $\sim 9 \times 10^{14} \text{ W/cm}^2$. (c) Measured neutron-averaged areal density as a function of peak drive intensity with continuous (diamonds) and double-picket (circles) pulses. (d) Hard x-ray signal as a function of peak drive intensity with continuous (diamonds) and double-picket (circles) pulses.

By increasing the peak intensity in the continuous-pulse implosions, the areal density did not increase, shown by the diamonds in Fig. 117.16(c). As discussed in the previous section, the shocks were not properly timed in these implosions, resulting in a decrease of the measured compression. The better-timed, double-picket implosions produced higher compression with areal densities up to $\sim 150 \text{ mg/cm}^2$ at high peak intensities, shown by the open circles [Fig. 117.16(c)]. Variations in these data are caused by variations in the picket energies and uncertainties for the shock-timing experiments. These multiple-picket designs are being optimized in current campaigns. Figure 117.16(d) presents the measured hard x-ray signal, produced by hot electrons from TPD instability, as a function of peak intensity for both types of drive pulses. The hard x-ray signal increases with peak intensity.²⁴ The preheat energy, which is estimated based on the measured hard x-ray signal, is of the order of $\sim 20 \text{ J}$ in the high-intensity implosions.⁴ This corresponds to $\sim 0.1\%$ of the total laser energy.⁴ With such levels of preheat, the areal density is expected to

be reduced from $\sim 250 \text{ mg/cm}^2$ to $\sim 210 \text{ mg/cm}^2$, if shock timing is optimized. These levels of preheat should not preclude obtaining an ignition-relevant areal density of $\sim 200 \text{ mg/cm}^2$ at peak intensities of $\sim 1 \times 10^{15} \text{ W/cm}^2$. The fact that the measured compression is below this level suggests that shock timing still must be improved and/or the hot-electron preheat is larger than previously estimated. Future experiments with both triple-picket pulse shapes and high-Z ablaters will address the most important issues in the direct-drive program.

Preheat

An important source of compression degradation is the shell preheat caused by hot electrons generated by TPD instability.^{4,18,19,24} This preheat was shown to be virulent in DT and D₂ ablaters^{4,24} and was reduced by using plastic ablaters.^{4,5} As a result, the highest, ignition-relevant areal densities with shell ρR of $\sim 200 \text{ mg/cm}^2$ were achieved in cryogenic D₂-fuel implosions with plastic ablaters when the hot-electron preheat was reduced to zero, at a moderate laser-drive peak intensity of

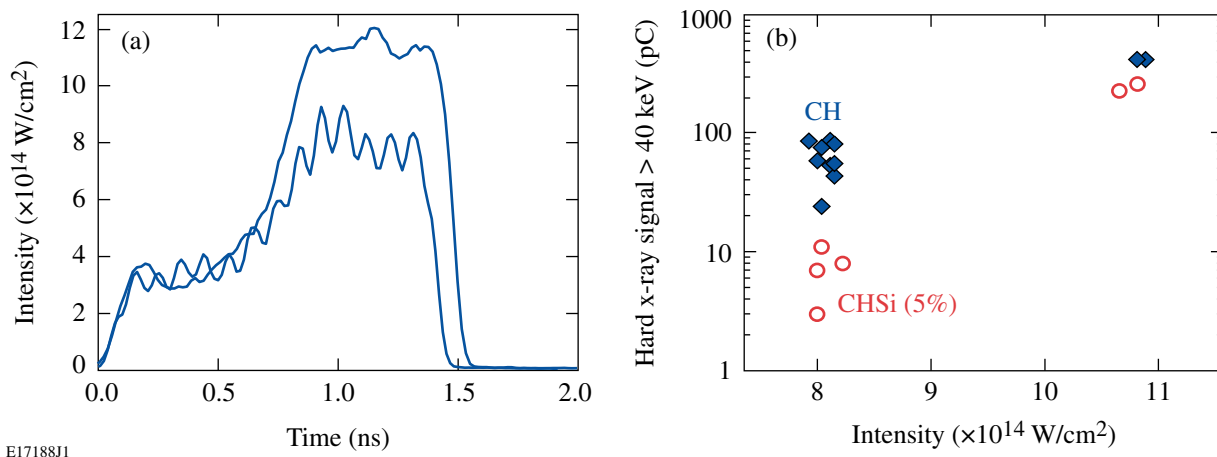
$\sim 5 \times 10^{14}$ W/cm² (Ref. 5). By increasing the peak intensity to $\sim 1 \times 10^{15}$ W/cm², the implosion velocity can be raised to levels required for ignition, but hard x-ray signals, associated with TPD hot electrons, also increase,²⁴ as shown in Fig. 117.16(d). While current hot-electron preheat estimates in plastic-ablator OMEGA implosions (with the estimated cold-shell preheat-energy fraction approaching $\sim 0.1\%$ of the total laser energy) do not preclude achieving ignition-relevant compression (with shell ρR of ~ 200 mg/cm²) at high peak intensities of $\sim 1 \times 10^{15}$ W/cm² and an initial shell adiabat of $\alpha \sim 2$ (Ref. 4), the longer plasma scale lengths in NIF targets make them potentially more vulnerable to hot-electron production than OMEGA targets.²⁴ While there are no reliable predictive capabilities for hot-electron preheat due to the very complex nature of nonlinear TPD instability, higher-Z ablaters are expected to mitigate the hot-electron preheat compared to the plastic ablaters. Plastic ablaters with 5% by atom of Si dopant were used recently²⁵ for this purpose.

Figure 117.17 shows a comparison of the hard x-ray signals measured in plastic and Si-doped plastic implosions. The implosions were performed with shaped pulses in which the peak intensity varied from ~ 0.8 to $\sim 1.1 \times 10^{15}$ W/cm² and a drive energy from ~ 18 to ~ 27 kJ. Two representative pulse shapes are shown in Fig. 117.17(a). The plastic and Si-doped plastic shells were $27 \mu\text{m}$ thick, and the concentration of Si dopant in plastic shells was 5% by atom. The comparison of the measured hard x-ray signals in the >40 -keV range [Fig. 117.17(b)] shows that the signals grow exponentially with the drive energy in CH implosions as drive energy increases. The signals were reduced in Si-doped CH shells at low drive energies; the reduction was $\sim 1.5\times$ at higher drive energies and peak intensities of $\sim 1.1 \times$

10^{15} W/cm². Future experiments will use higher-Z ablaters to further reduce hot-electron preheat.

Conclusions

This article has reviewed progress in cryogenic-implosion physics on OMEGA. After achieving ignition-relevant areal densities of ~ 200 mg/cm² in cryogenic-D₂ implosions at peak laser-drive intensities of $\sim 5 \times 10^{14}$ W/cm², the focus of the program has been on understanding the compression physics at peak laser-drive intensities of $\sim 1 \times 10^{15}$ W/cm² that are required to achieve ignition-relevant implosion velocities. Acceleration experiments showed the importance of the non-local electron-thermal-transport effects in modeling the laser drive. The nonlocal, hot-electron preheat was shown to stabilize Rayleigh–Taylor growth at a peak drive intensity of $\sim 1 \times 10^{15}$ W/cm². The measured compressibility of plastic targets driven with high-compression, shaped pulses agrees well with 1-D predictions. Shock mistiming has been shown to be an important mechanism in compression degradation of recent cryogenic implosions driven with continuous pulses. Cryogenic implosions driven with double-picket pulses, which are easier to tune than continuous pulses, demonstrate an improvement in compression performance at a peak drive intensity of $\sim 1 \times 10^{15}$ W/cm². The shell preheat caused by hot electrons generated by two-plasmon-decay instability was reduced by using Si-doped ablaters. Future experiments will investigate higher-Z ablaters (such as glass or Si) for further hot-electron preheat reduction. Significant progress in understanding ignition-relevant cryogenic target implosions has been made on OMEGA since the publication of Ref. 4.



E17188J1

Figure 117.17

(a) Two representative pulse shapes used to implode $27\text{-}\mu\text{m}$ -thick plastic shells and Si-doped (5% by atom) plastic shells. (b) Hard x-ray signals measured in plastic (diamonds) and Si-doped (circles) implosions.

ACKNOWLEDGMENT

This work was supported by the U.S. Department of Energy Office of Inertial Confinement Fusion under Cooperative Agreement No. DE-FC52-08NA28302, the University of Rochester, and the New York State Energy Research and Development Authority. The support of DOE does not constitute an endorsement by DOE of the views expressed in this article.

REFERENCES

1. S. Atzeni and J. Meyer-ter-Vehn, *The Physics of Inertial Fusion: Beam Plasma Interaction, Hydrodynamics, Hot Dense Matter*, International Series of Monographs on Physics (Clarendon Press, Oxford, 2004).
2. J. D. Lindl, *Inertial Confinement Fusion: The Quest for Ignition and Energy Gain Using Indirect Drive* (Springer-Verlag, New York, 1998).
3. S. E. Bodner *et al.*, Phys. Plasmas **7**, 2298 (2000).
4. R. L. McCrory, D. D. Meyerhofer, R. Betti, R. S. Craxton, J. A. Delettrez, D. H. Edgell, V. Yu. Glebov, V. N. Goncharov, D. R. Harding, D. W. Jacobs-Perkins, J. P. Knauer, F. J. Marshall, P. W. McKenty, P. B. Radha, S. P. Regan, T. C. Sangster, W. Seka, R. W. Short, S. Skupsky, V. A. Smalyuk, J. M. Soures, C. Stoeckl, B. Yaakobi, D. Shvarts, J. A. Frenje, C. K. Li, R. D. Petrasso, and F. H. Séguin, Phys. Plasmas **15**, 055503 (2008).
5. T. C. Sangster, V. N. Goncharov, P. B. Radha, V. A. Smalyuk, R. Betti, R. S. Craxton, J. A. Delettrez, D. H. Edgell, V. Yu. Glebov, D. R. Harding, D. Jacobs-Perkins, J. P. Knauer, F. J. Marshall, R. L. McCrory, P. W. McKenty, D. D. Meyerhofer, S. P. Regan, W. Seka, R. W. Short, S. Skupsky, J. M. Soures, C. Stoeckl, B. Yaakobi, D. Shvarts, J. A. Frenje, C. K. Li, R. D. Petrasso, and F. H. Séguin, Phys. Rev. Lett. **100**, 185006 (2008).
6. S. X. Hu, V. A. Smalyuk, V. N. Goncharov, S. Skupsky, T. C. Sangster, D. D. Meyerhofer, and D. Shvarts, Phys. Rev. Lett. **101**, 055002 (2008).
7. Y. Lin, T. J. Kessler, and G. N. Lawrence, Opt. Lett. **20**, 764 (1995).
8. T. R. Boehly, V. A. Smalyuk, D. D. Meyerhofer, J. P. Knauer, D. K. Bradley, R. S. Craxton, M. J. Guardalben, S. Skupsky, and T. J. Kessler, J. Appl. Phys. **85**, 3444 (1999).
9. S. P. Regan, J. A. Marozas, J. H. Kelly, T. R. Boehly, W. R. Donaldson, P. A. Jaanimagi, R. L. Keck, T. J. Kessler, D. D. Meyerhofer, W. Seka, S. Skupsky, and V. A. Smalyuk, J. Opt. Soc. Am. B **17**, 1483 (2000).
10. R. C. Malone, R. L. McCrory, and R. L. Morse, Phys. Rev. Lett. **34**, 721 (1975).
11. V. N. Goncharov, O. V. Gotchev, E. Vianello, T. R. Boehly, J. P. Knauer, P. W. McKenty, P. B. Radha, S. P. Regan, T. C. Sangster, S. Skupsky, V. A. Smalyuk, R. Betti, R. L. McCrory, D. D. Meyerhofer, and C. Cherfils-Clérouin, Phys. Plasmas **13**, 012702 (2006).
12. S. G. Glendinning, S. N. Dixit, B. A. Hammel, D. H. Kalantar, M. H. Key, J. D. Kilkenny, J. P. Knauer, D. M. Pennington, B. A. Remington, R. J. Wallace, and S. V. Weber, Phys. Rev. Lett. **78**, 3318 (1997).
13. H. Azechi *et al.*, Phys. Plasmas **4**, 4079 (1997).
14. V. A. Smalyuk, S. X. Hu, V. N. Goncharov, D. D. Meyerhofer, T. C. Sangster, D. Shvarts, C. Stoeckl, B. Yaakobi, J. A. Frenje, and R. D. Petrasso, Phys. Rev. Lett. **101**, 025002 (2008).
15. V. A. Smalyuk, S. X. Hu, V. N. Goncharov, D. D. Meyerhofer, T. C. Sangster, C. Stoeckl, and B. Yaakobi, Phys. Plasmas **15**, 082703 (2008).
16. R. Betti, V. N. Goncharov, R. L. McCrory, and C. P. Verdon, Phys. Plasmas **5**, 1446 (1998).
17. Y. C. Lee and P. K. Kaw, Phys. Rev. Lett. **32**, 135 (1974).
18. C. S. Liu and M. N. Rosenbluth, Phys. Fluids **19**, 967 (1976).
19. C. Stoeckl, R. E. Bahr, B. Yaakobi, W. Seka, S. P. Regan, R. S. Craxton, J. A. Delettrez, R. W. Short, J. Myatt, A. V. Maximov, and H. Baldis, Phys. Rev. Lett. **90**, 235002 (2003).
20. S. X. Hu, V. A. Smalyuk, V. N. Goncharov, J. P. Knauer, P. B. Radha, I. V. Igumenshchev, J. A. Marozas, C. Stoeckl, B. Yaakobi, D. Shvarts, T. C. Sangster, P. W. McKenty, D. D. Meyerhofer, S. Skupsky, and R. L. McCrory, Phys. Rev. Lett. **100**, 185003 (2008).
21. T. R. Boehly, D. H. Munro, P. M. Celliers, R. E. Olson, D. G. Hicks, V. N. Goncharov, G. W. Collins, H. F. Robey, S. X. Hu, J. A. Marozas, T. C. Sangster, O. L. Landen, and D. D. Meyerhofer, Phys. Plasmas **16**, 056302 (2008).
22. P. M. Celliers, D. K. Bradley, G. W. Collins, D. G. Hicks, T. R. Boehly, and W. J. Armstrong, Rev. Sci. Instrum. **75**, 4916 (2004).
23. V. A. Smalyuk, R. Betti, J. A. Delettrez, V. Yu. Glebov, V. N. Goncharov, D. Y. Li, D. D. Meyerhofer, S. P. Regan, S. Roberts, T. C. Sangster, C. Stoeckl, W. Seka, J. A. Frenje, C. K. Li, R. D. Petrasso, and F. H. Séguin, Phys. Plasmas **14**, 022702 (2007).
24. V. A. Smalyuk, D. Shvarts, R. Betti, J. A. Delettrez, D. H. Edgell, V. Yu. Glebov, V. N. Goncharov, R. L. McCrory, D. D. Meyerhofer, P. B. Radha, S. P. Regan, T. C. Sangster, W. Seka, S. Skupsky, C. Stoeckl, B. Yaakobi, J. A. Frenje, C. K. Li, R. D. Petrasso, and F. H. Séguin, Phys. Rev. Lett. **100**, 185005 (2008).
25. J. P. Knauer, P. B. Radha, V. N. Goncharov, I. V. Igumenshchev, R. Betti, R. Epstein, F. J. Marshall, S. P. Regan, V. A. Smalyuk, D. D. Meyerhofer, and S. Skupsky, Bull. Am. Phys. Soc. **52**, 233 (2007).